*Article*

# Ionic Conductivity of Lithium Phosphides

Alexey P. Maltsev, Ilya V. Chepkasov *, Alexander G. Kvashnin and Artem R. Oganov

Skolkovo Institute of Science and Technology, Bolshoy Boulevard 30, bld. 1, Moscow 121205, Russia; alexey.maltsev@skoltech.ru (A.P.M.); a.kvashnin@skoltech.ru (A.G.K.); a.oganov@skoltech.ru (A.R.O.)
* Correspondence: i.chepkasov@skoltech.ru

**Abstract:** We comprehensively study the ionic conductivity in lithium phosphides, promising materials for energy storage applications, by using a combination of first-principles computations and machine learning interatomic potentials. Using the quasiharminic approximation, we calculated convex hulls of the Li-P system at various temperatures and the temperature-composition phase diagram was obtained, delineating the stability regions of each phase. The ionic conductivity of stable ($Li_3P$, $LiP$, $Li_3P_7$, $Li_3P_{11}$, $LiP_7$) and metastable ($Li_4P_3$, $Li_5P_4$, $LiP_5$) compounds was studied as a function of temperature. In some compounds we found have high ionic conductivity at room temperatures ($10^{-3}$–$10^{-2}$ S cm$^{-1}$). Structures with the lowest ionic conductivity are $LiP$, $Li_3P_{11}$, and $LiP_7$, in which diffusion is negligible in the whole temperature range 300–500 K. In $Li_3P$, $Li_3P_7$, and $Li_4P_3$, $LiP$, there is the 3D diffusion of Li atoms, while in $Li_5P_4$ the 2D mechanism prevails, and in $LiP_5$ and $LiP_7$ the 1D mechanism was observed. This study may provide insights for the development of Li-P materials in lithium ion and lithium metal battery applications.

**Keywords:** ionic conductivity; lithium phosphides; density functional theory; machine learning interatomic potential; molecular dynamics

## 1. Introduction

Lithium ion batteries (LIB) are widely used [1–9]: they are the most effective secondary energy sources for portable and mobile devices [10–16] and are also used in electric vehicles [17–20]. However, the maximum specific energy of modern commercial LIBs is about 250 Wh kg$^{-1}$ (theoretical capacity of Li in griphite anode is 372 mAh g$^{-1}$), which does not satisfy new needs [7,14,21–23]. To overcome the capacity limitations, the use of other anodes is suggested, such as Li-metal anode [2–5], or different lithium alloys [24], i.e., silicon anodes have the highest capacity of 3579 mAh g$^{-1}$ [25]. The main problems with lithium ion, and especially Li-metal batteries, are dendrite formation and/or large structural changes under lithiation [24,25], leading to poor cyclability, a lower Coulomb efficiency, reduced service life, and short circuits [26]. There are several ways to solve these problems. Safety and durability can be improved by switching from liquid to solid electrolytes, more effectively preventing dendrite formation and short circuits, and thus increasing the safety and cyclability of batteries [21,27,28]. Moreover, the transition to all-solid-state batteries will allow for the use of lithium metal instead of a graphite anode, which will increase the specific capacity of batteries [14,21].

A solid electrolyte, just like a liquid one, must be a good ionic conductor and should not conduct electrons, be thermally stable and, when in contact with the anode, must form stable solid interphases, which must also be good ionic conductors and mechanically and thermally stable [21].

Li-P-S compounds are promising candidates for the role of a solid electrolyte in batteries with a metal lithium anode. For example, batteries with $Li_2S$-$P_2S_5$ electrolyte were assembled and tested, their interfacial layers with lithium were studied, and the mechanisms of dissolution and precipitation of lithium in $Li_2S$-$P_2S_5$ were determined using scanning electron microscopy methods [29–31]. Liu et al. [32] studied the effect of

microstructure modification on the ionic conductivity of $Li_3PS_4$ and showed the possibility of its use at room temperature. Li-P-S compounds and the interfacial layers they form in contact with lithium were also studied by first-principles simulations. It was shown [33] that the $Li_3PS_4$-$Li_3PO_4$ electrolyte forms interfacial layers $Li_3PS_4$, $Li_3PO_4$, $Li_2O$, $Li_2S$, of which $Li_3PO_4$ is the least stable. In more complex systems, such as $Li_7P_3S_{11}$, the ionic conductivity varies from $10^{-5}$ to $10^{-3}$ S cm$^{-1}$ depending on the morphology [34], and substitution by iodine [35] or other halogens [36] can lead to an increase in ionic conductivity and improve the stability of these solid-state electrolytes.

In some studies, phosphides or even phosporous materials are considered promising anode materials [37–41] because of their high theoretical capacity and low redox potentials, i.e., 2596 mAh g$^{-1}$ for $Na_3P$ [42]. Amine et al. proposed using a composite material based on black phosphorous and showed that ball milling modification helps to achieve a high initial Coulomb efficiency, high reversible capacity and good electrochemical performance [43]. Fang et al. developed a composite phosphorous anode for Na-ion batteries with a high reversible capacity and great electrochemical performance [44]. A hierarchical red phosphorous composite anode for K-ion batteries was designed and showed a high reversible capacity of 566.7 mAh g$^{-1}$ after 100 cycles at 0.1 A g$^{-1}$ and long cycling stability [45]. Despite the rapid growth of research and recent progress, there are still many unresolved issues that need attention. From this point of view, a complex investigation of the stability and ionic conductivity of all possible compounds in Li-P is essential.

A search for the most stable and the best ionic conductor among Li-P compounds will help to improve existing lithium-based batteries and develop an efficient liquid and solid sodium and potassium ion batteries. This work reports an extensive computational search of all stable Li-P compounds and evaluation of their ionic conductivity by modern computational techniques.

## 2. Materials and Methods

All density functional theory (DFT) calculations were performed using Vienna Ab initio Simulation Package (VASP) [46,47] using the projector augmented-wave method [48] with a plane-wave basis set [49] and Perdew–Burke–Ernzerhof (PBE) exchange-correlation functional [50]. Energy cutoff was set at 500 eV. Gamma-centered k-points mesh with $2\pi \times 0.01$ Å$^{-1}$ spacing was used. Phonon were calculated using the supercell approach and the finite displacement method [51], as implemented in Phonopy package [52]. Ab Initio Molecular Dynamics (AIMD) [53], to collect datasets for the machine learning interatomic potential (MLIP), was run at 1000 K with NPT ensemble and Langevin thermostat [54,55].

Moment tensor potential (MTP) was used as an MLIP. The MTP potentials are non-parametric potentials that use linear regression and invariant polynomials [56]. They are based on tensors of inertia of atomic environments and can approximate any regular function with the necessary symmetries. MTP potentials are up to 150 times faster than GAP potentials with the same magnitude of force RMS error and up to 50 times faster, with an error that is 1.5 times smaller than GAP [56,57]. The MLIP code, which allows for active learning with MTP, has been successfully used in many applications, including a crystal structure search, phase transitions, phase diagram prediction, and thermodynamic and kinetic properties [58–63].

MLIP was constructed using MLIP-3 package [64,65] in several stages. At the first stage [56], MTP of the 20th level was pretrained using data collected from AIMD. A total of 24,000 configurations from AIMD calculations were collected, and each 100th configuration was taken for the initial MLIP. At the second stage, 240 unique configurations from the AIMD-dataset were added using *select-add* function of MLIP-3 package. At the final stage, eight consecutive active learning [58,65] procedures were performed for each structure on the convex hull (or low-lying metastable phases). The extrapolation threshold and threshold-brake grade parameters were set to 2.0 and 35.0, respectively. Molecular dynamics simulations for the active learning were performed in LAMMPS [66,67] code;

structures were collected during heating from 0 K to 1000 K with a heating rate $2 \times 10^6$ K s$^{-1}$ and annealing at 1000 K for 10 ns.

The accuracy of the constructed MLIP is shown in Table 1 and Figures 1–3. Root mean square (RMS) errors in energies per atom and forces predicted by MLIP are less than 0.019 eV/atom and 0.34 eV/Å, respectively, for the training set. RMS errors in energies and forces for the validation set are 0.012 eV/atom and 0.145 eV/Å.

**Table 1.** Errors of the MLIP. MEA, AAD and RMS denote maximal absolute difference, average absolute difference and RMS absolute difference, respectively, between DFT and MLIP data of the training set.

| Number of configurations | 1047 | | |
|---|---|---|---|
| | MAE | AAD | RMS |
| Errors in energy per atom, eV/atom | 0.063 | 0.0145 | 0.0185 |
| Range of energies per atom in training set , eV/atom | −5.09: −3.20 | | |
| Errors in forces, eV/ Å | 1.97 | 0.27 | 0.335 |
| Range of forces in training set, eV/ Å | −10.86: +18.18 | | |
| Errors in stresses, kBar | 37.76 | 5.576 | 8.0 |
| Range of stresses in training set , kBar | −84.1: +98.2 | | |
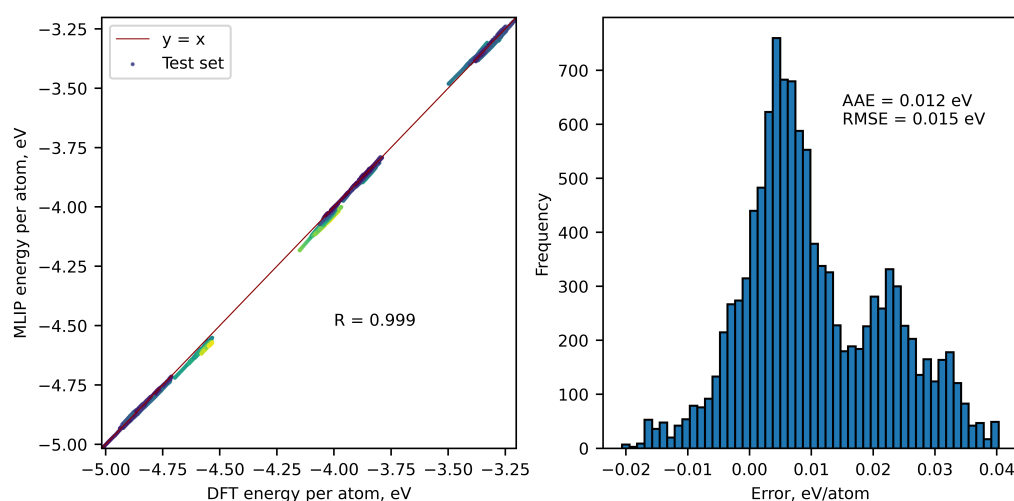


**Figure 1.** Energy errors on the validation data set and their distribution over the 11,311 configurations. AAE and RMSE denote average absolute error and RMS error, respectively, between DFT and MLIP data of the validation set.

Ionic conductivity was simulated using LAMMPS at temperatures 300–500 K with the step of 50 K for supercells with 5% vacancies on lithium sites. The size of the supercells was chosen so the number of atoms was approximately equal to 1000 and lattice parameters was close to 3 nm (See Table 2). Each simulation in LAMMPS was performed with NPT ensemple and Nose–Hoover thermostat [68,69] with a 0.5 fs timestep for 0.5 ns.
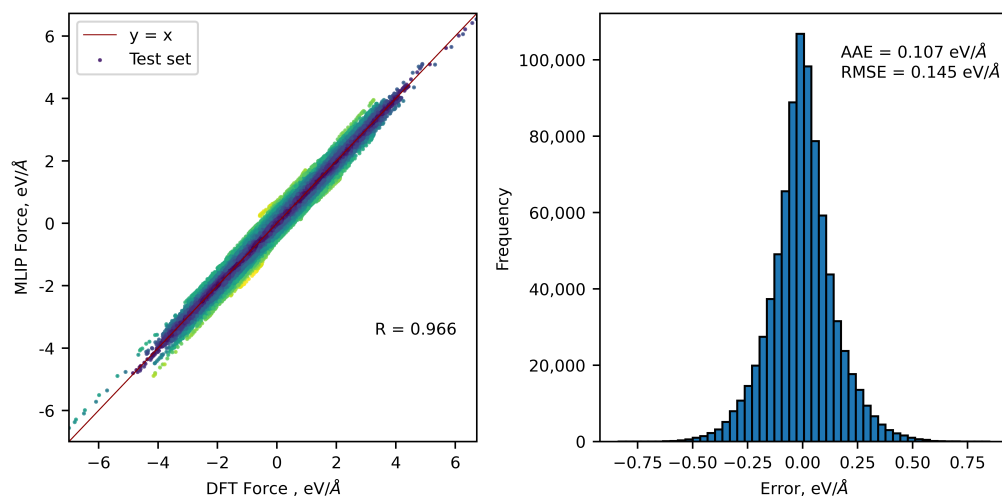
**Figure 2.** Force errors on the validation data set and their distribution over the 11,311 configurations (838,824 values of force components). AAE and RMSE denote average absolute error and RMS error, respectively, between DFT and MLIP data of the validation set.
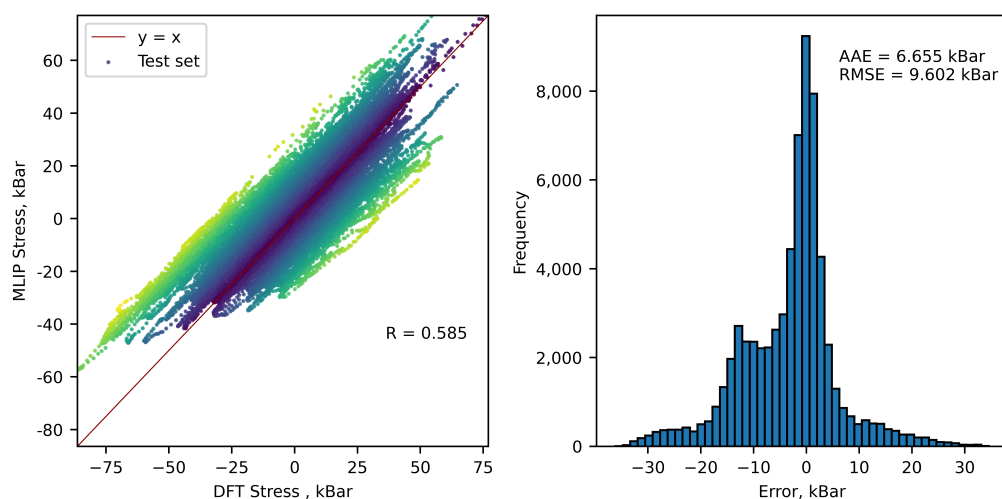


**Figure 3.** Stress errors on the validation data set and their distribution over the 11,311 configurations (67,866 values of stress components). AAE and RMSE denote average absolute error and RMS error, respectively, between DFT and MLIP data of the validation set.

**Table 2.** Details of supercells. N denotes number of atoms in the supercell.

|  | **Super Cell** | **Lattice Parameters** | | | | | | **N** |
|---|---|---|---|---|---|---|---|---|
|  |  | **a, Å** | **b, Å** | **c, Å** | **α, deg** | **β, deg** | **γ, deg** |  |
| $Li_3P$ | $6 \times 6 \times 3$ | 25.36 | 25.36 | 22.66 | 90 | 90 | 120 | 864 |
| $Li_3P_7$ | $4 \times 3 \times 3$ | 30.52 | 29.63 | 31.71 | 90 | 90 | 90 | 1440 |
| $Li_3P_{11}$ | $3 \times 5 \times 5$ | 39.33 | 30.21 | 33.94 | 90 | 118.95 | 90 | 1680 |
| $Li_4P_3$ | $2 \times 7 \times 3$ | 22.33 | 27.17 | 30.52 | 90 | 90 | 90 | 1176 |
| $Li_5P_4$ | $3 \times 7 \times 3$ | 26.59 | 27.84 | 25.45 | 90 | 109.37 | 90 | 1134 |
| $LiP$ | $5 \times 5 \times 3$ | 27.975 | 24.82 | 30.77 | 90 | 118.16 | 90 | 1200 |
| $LiP_5$ | $3 \times 5 \times 4$ | 31.45 | 33.39 | 26.7 | 90 | 90 | 90 | 1440 |
| $LiP_7$ | $2 \times 2 \times 2$ | 27.29 | 27.29 | 29.74 | 90 | 90 | 90 | 1024 |

Diffusion coefficients were calculated using mean square displacements (MSD) of $Li^+$ cations:

$$D = \frac{1}{6} \lim_{t \to \infty} \frac{d}{dt} \frac{1}{N} \sum_{i=1}^{N} < |r_i(t) - r_i(0)|^2 > \tag{1}$$

Activation energy $E_a$ was calculated using Arrhenius formula:

$$D = D_0 exp(\frac{-E_a}{k_B T}) \tag{2}$$

The ionic conductivity of lithium was calculated using Nernst–Einstein formula:

$$\sigma = \frac{nq^2 D}{H_r k_B T} \tag{3}$$

where $n$ is the $Li^+$ ion density, $q$ is the formal charge of the lithium ($q = 1$), $k_B$ is Boltzmann constant, $T$ is the temperature and $H_r$ is Haven ratio (assumed to be 1).

## 3. Results and Discussion

Before calculations of ionic conductivity in Li-P systems, we collected information about known stable and metastable Li-P compounds. Computational databases have different information about the stability of various structures. For example, in the OQMD [70,71] database, $Li_3P_{11}$ appears to be stable, while in thr Materials Project [72] database, this structure is not presented at all. Mayo et al. [37] performed first-principles structure prediction and showed that $Li_3P_{11}$ is metastable. However, previously it was shown by Sen and Johari [73] that the methodology used by Mayo et al. [37,74] has led to incorrect results in similar systems. Later, Fei et al. [75] reported that $Li_5P_2$ and $Li_4P$ became stable under high pressures and could be observed at ambient conditions. In order to understand which compounds are stable, we recalculated all known Li-P structures and studied their thermodynamic stability. We also carried out USPEX [76–78] calculations in order to predict previously unknown Li-P structures. More than 70 generations of 200 structures each were calculated. We did not find new stable or low-lying metastable phases.

The stability of Li-P compounds was analyzed by the calculation and construction of the convex hull, as shown in Figure 4a. Zero-point energy (ZPE) contribution was taken into account during the calculation of the convex hull. We found seven phases on the convex hull, namely $Li - Im\bar{3}m$, $Li_3P - P6_3/mmc$, [79] $LiP - P2_1/c$, [80] $Li_3P_7 - P2_12_12_1$, [81] $Li_3P_{11} - Cm$, $LiP_7 - I4_1/acd$, [82] $P - Cmca$ (black phosphorous).

Experimentally known $LP_5 - Pnma2_1$ [82] is 16 meV/atom above the convex hull according to our DFT calculations. Mayo et al. [37] predicted that $Li_4P_3 - P2_12_12_1$ was close to the convex hull and was dynamically stable, i.e. had no imaginary phonon frequencies. In our calculation, the $Li_4P_3 - P2_12_12_1$ phase is 4 meV/atom above the convex hul; see Figure 4a. $Li_5P_4 - C2/m$ was constructed using $Na_5As_4$ [83] as a prototype and is also very close to the convex hull (9 meV/atom). Fei et al. [75] predicted two stable compounds, $Li_5P_2 - P3m1$ and $Li_4P - R\bar{3}m$, claiming that they become stable at high pressure and can be observed at ambient conditions. According to our calculations, $Li_5P_2 - P3m1$ and $Li_4P - R\bar{3}m$ are 44 and 60 meV/atom above the convex hull, respectively.

We calculated phonon densities of states (PhDOS) for 20 stable and low-energy metastable structures shown in (Figure 4a). Integration over the phonon DOS allowed us to calculate the zero-point energy and vibrational contribution to the Helmholtz free energy for all studied compounds and construct the convex hulls at finite temperatures. Stability of the predicted compounds at different temperatures is summarized in the composition–temperature phase diagram (Figure 4b). Our calculations show that at temperatures higher than 550 K, $Li_3P_{11} - Cm$ becomes metastable; $Li_5P_4 - C2/m$, on the other hand, becomes stable at T = 700 K and appears on the convex hull.
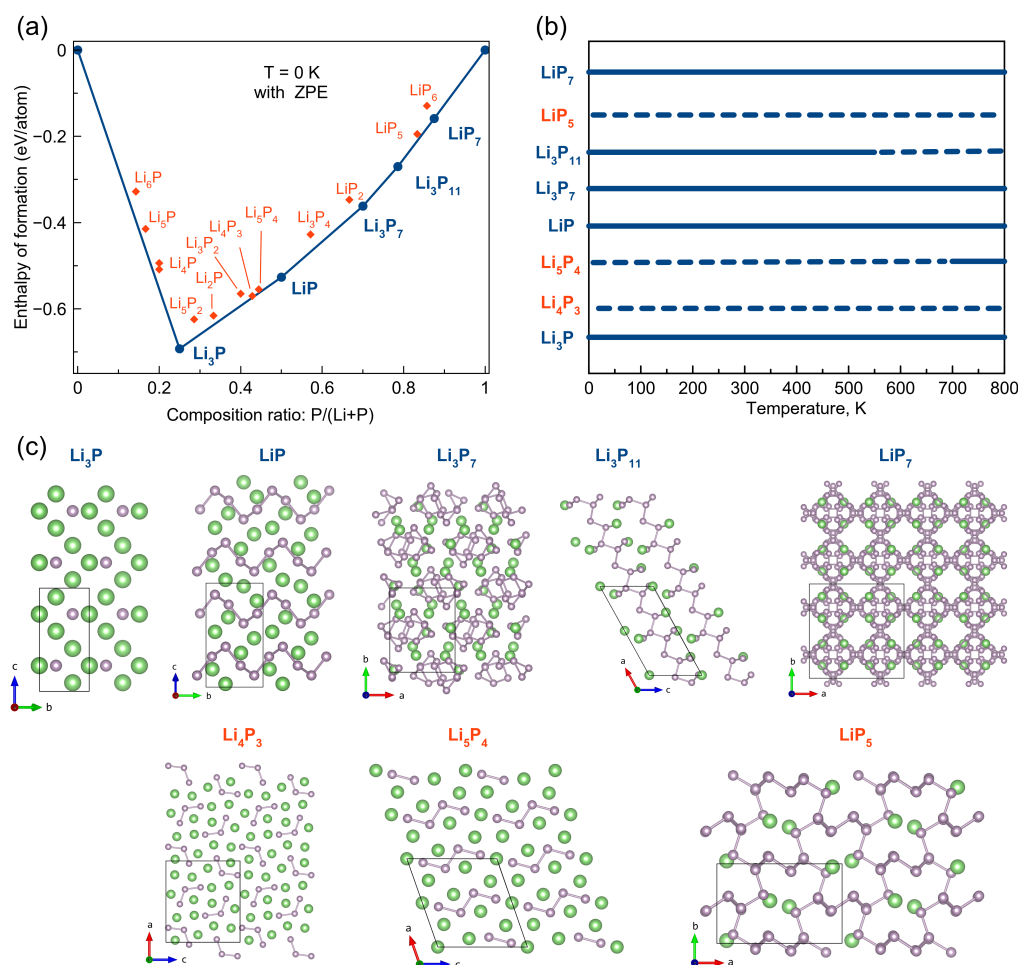
**Figure 4.** (**a**) Calculated convex hull of the Li-P system at T = 0 K with ZPE. Blue circles represent stable compounds; red diamonds show metastable structures. (**b**) Composition–temperature phase diagram; solid line shows temperature region where the structure is stable, while the dashed line shows regions where the structure is metastable. (**c**) Crystal structures of considered Li-P compounds; big green atoms and small purple atoms are Li and P, respectively.

All $Li_xP$ structures can be classified into four categories according to the arrangement of P atoms [37]: (1) $0 \leq x \leq 0.5$: tubes, cages, 3-D network—$LiP_7$, $LiP_6$, $LiP_5$, $Li_3P_{11}$, $Li_3P_7$; (2) $0.5 \leq x \leq 1.33$: infinite or finite chains—$LiP_2$, $Li_3P_4$, $LiP$, $Li_5P_4$, $Li_4P_3$; (3) $1.33 \leq x \leq 2$: P dumbbells—$Li_3P_2$, $Li_2P$, $Li_5P_2$; (4) $1.33 \leq x \leq 2$: isolated P ions—$Li_3P$, $Li_4P$, $Li_5P$, $Li_6P$. We discuss below how structural topology affects the ionic conductivity.

Figure 5 shows the ionic conductivity of stable systems ($Li_3P$, $LiP$, $Li_3P_7$, $Li_3P_{11}$, $LiP_7$) and low-lying metastable phases ($Li_4P_3$, $Li_5P_4$, $LiP_5$) with 5% vacancy concentration as a function of temperature. Most structures have high ionic conductivity at room temperature about $10^{-3}$–$10^{-2}$ S cm$^{-1}$; however, for LiP, such values are obtained only at temperatures higher than 400 K, while in $LiP_7$ diffusion is negligible it the whole temperature range 300–500 K. Curiously, experimental data are controversial: Wegner et al. [84] found the ionic conductivity of $Li_3P$ to be $10^{-6}$–$10^{-4}$ S cm$^{-1}$, but in article [85] $10^{-4}$–$10^{-2}$ S cm$^{-1}$ at temperatures 300–500 K. We explain such divergence by differences in the microstructure of materials: Wegner et al. [84] studied cold-pressured material, while Nazri [85] studied polycrystalline material, which might have more defects and vacacies. Our results are in good agreement with the earlier work [85]. In a polycrystalline material, diffusion is enhanced at grain boundaries, which explains the difference. In our simulations, we see almost negligible ionic conductivity for most systems without vacancies; however, once vacancies are introduced, ionic conductivity can become very high.
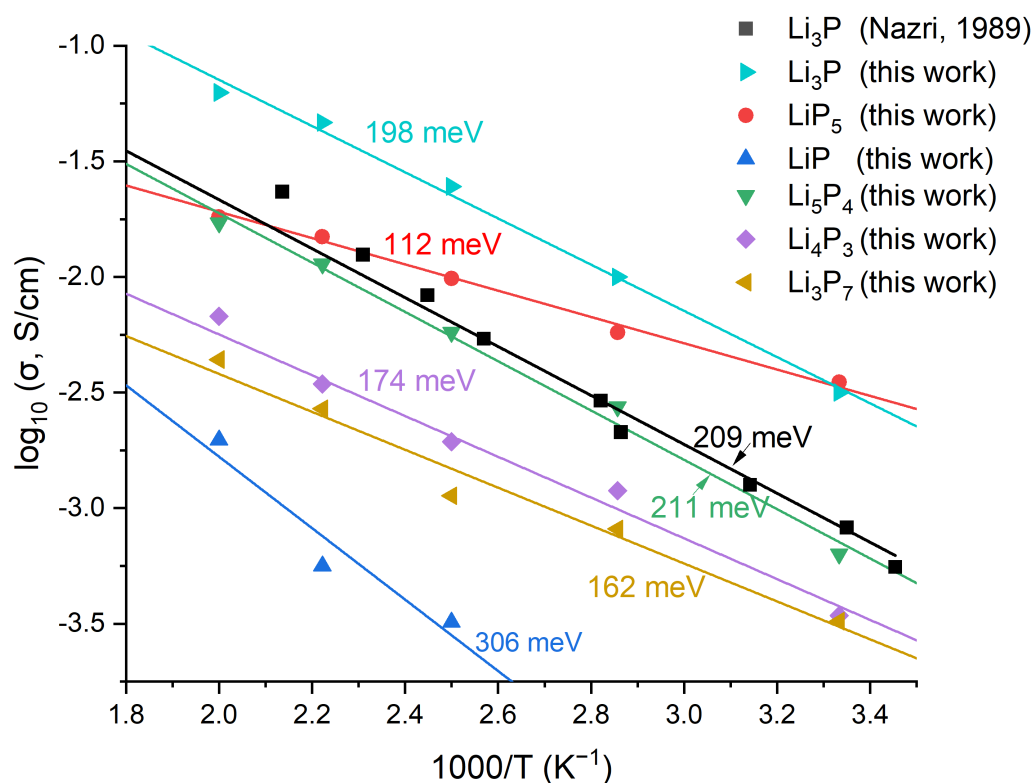
**Figure 5.** Calculated ionic conductivity of Li-P compounds as a function of temperature. Experimental ionic conductivities were taken from article [85] and refitted by us.

The trajectories of $Li^+$ diffusion are shown in Figure 6. $Li_3P$, $Li_3P_7$, $Li_4P_3$, LiP are 3D conductors, but in $Li_3P_7$, the diffusion of Li ions prevails along the z-direction: on the Li trajectory, there are screw chains, which are connected though x- and y- directions. In LiP, there are a few Li jumps and small amount of trajectories, indicating a low diffusion rate with high activation energy. $Li_5P_4$ is a 2D ionic conductor; trajectory lines are located along the x–y plane and correspond to the diffusion of Li atoms located between P-chain layers. Lithium atoms, which have strong bonds with the four-atom P-chains, do not diffuse, forming a non-conductive layer, and there are only a few, rare Li jumps from non-conductive to conductive layers. One-dimensional diffusion appears in structures with a 3D network of P atoms, so in 3D conductor $Li_3P_7$, 1D conductivity along the y-axis prevails and $LiP_5$ and $LiP_7$ are 1D conductors. In $LiP_7$, diffusion proceeds through two channels along the z-direction, which are connected to each other and form an extended cross; however, there are only a few trajectory lines, which appear only at elevated temperatures (500–600 K), indicating low diffusion and high activation energy; the ionic conductivity of $LiP_7$ at 500 K is about $10^{-3}$ S cm$^{-1}$ and negligible at lower temperatures. $Li_3P_{11}$ has dumbbell chains, which are not connected to each other; thus, no spatial diffusion is obtained. Our results indicate that not only does $Li_3P$ have high ionic conductivity, but almost all other stable and low-energy metastable phases (except $Li_3P_{11}$ and $LiP_7$).

Li₃P (3D)  Li₃P₇ (3D)  Li₄P₃ (3D)  LiP (3D)

Li₅P₄ (2D)  LiP₅ (1D)  LiP₇ (1D)  Li₃P₁₁ (0D)
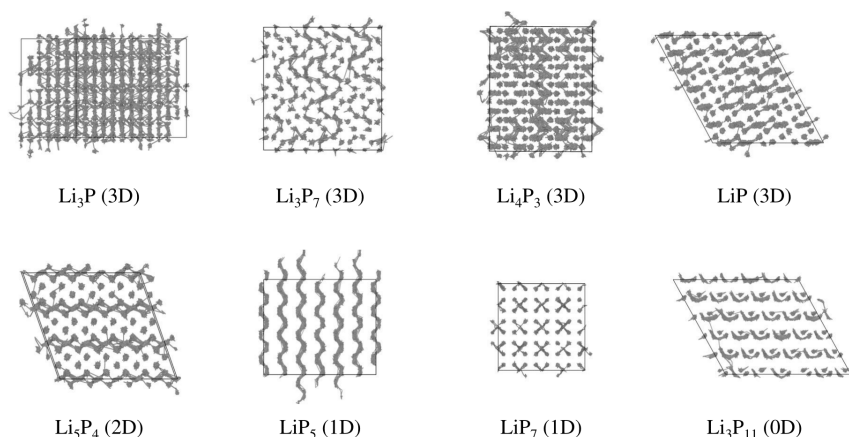
**Figure 6.** Calculated trajectories of Li-ion diffusion and their topology (in parentheses). For a better representation, ions are not shown. Trajectories were collected at 600 K for 0.2 ns after 0.1 ns heating.

## 4. Conclusions

We performed an extensive study of lithium–phosphorous compounds as promising candidates for solid-state electrolytes, anodes or components of electrolyte interphase in Li-ion or Li-metal batteries. Our first-principles calculations allowed us to determine the stability regions of all considered structures in the temperature range from 0 to 700 K. We found that $Li_3P - P6_3/mmc$, $LiP - P2_1/c$, $Li_3P_7 - P2_12_12_1$, $Li_3P_{11} - Cm$, $LiP_7 - I4_1/acd$ are stable at room temperature, while at temperatures higher than 550 K $Li_3P_{11}$ becomes metastable, and at temperatures higher than 700 K $Li_5P_4$ becomes stable. Our results indicate a variety of metastable compounds, some of which might exist at solid electrolyte interphase during battery operation. The diffusion of Li atoms was studied using molecular dynamics simulations with machine learning interatomic potentials. High lithium diffusion was observed for $Li_3P$, $LiP_5$, $Li_5P_4$, $Li_4P_3$, and $Li_3P_7$, and their ionic conductivity was in the range $10^{-4}$–$10^{-2}$ S cm$^{-1}$ at room temperature. We also determined the qualitative dependence of ionic conductivity on the arrangement of phosphorous atoms; namely, the compounds with a 3D network of phosphorus possess 1D conductivity ($LiP_5$ and $LiP_7$), compounds with phosphorus chains or broken chains display a 2D type of conductivity (i.e., $Li_5P_4$), while other arrangements lead to 3D conductivity. Lithium phosphides are a promising class of electrolytes for lithium metal batteries.

**Data Availability Statement:** Zip-archive, containing folders *Diffusion trajectories* and *MLIP-DFT data*. *Diffusion trajectories* is the folder with diffusion trajectories, calculated at 600 K using LAMMPS. *MLIP-DFT* data is the folder with interatomic potentials files *p.mtp* and *mlip.ini*, *training_dft.cfg*—final data set for the training of the MLIP, *training_mlp.cfg*—file with configuration obtained from DFT calculations with recalculated using MLIP enrgies, forces and stresses, *validation_dft.cfg* and *validation_mlp.cfg* files, which contain validation data set configurations obtained from DFT calculations and recalculated using MLIP.

**Conflicts of Interest:** The authors declare no conflict of interest.

## References

1. Marom, R.; Amalraj, S.F.; Leifer, N.; Jacob, D.; Aurbach, D. A review of advanced and practical lithium battery materials. *J. Mater. Chem.* **2011**, *21*, 9938–9954. [CrossRef]
2. Nazri, G.A.; Pistoia, G. *Lithium Batteries: Science and Technology*; Springer Science & Business Media: Berlin/Heidelberg, Germany, 2008.
3. Girishkumar, G.; McCloskey, B.; Luntz, A.C.; Swanson, S.; Wilcke, W. Lithium- air battery: Promise and challenges. *J. Phys. Chem. Lett.* **2010**, *1*, 2193–2203. [CrossRef]
4. Scrosati, B.; Garche, J. Lithium batteries: Status, prospects and future. *J. Power Sources* **2010**, *195*, 2419–2430. [CrossRef]
5. Armand, M.; Tarascon, J.M. Building better batteries. *Nature* **2008**, *451*, 652–657. [CrossRef] [PubMed]
6. Kim, T.H.; Park, J.S.; Chang, S.K.; Choi, S.; Ryu, J.H.; Song, H.K. The current move of lithium ion batteries towards the next phase. *Adv. Energy Mater.* **2012**, *2*, 860–872. [CrossRef]
7. Goodenough, J.B.; Park, K.S. The Li-ion rechargeable battery: A perspective. *J. Am. Chem. Soc.* **2013**, *135*, 1167–1176. [CrossRef]
8. Etacheri, V.; Marom, R.; Elazari, R.; Salitra, G.; Aurbach, D. Challenges in the development of advanced Li-ion batteries: A review. *Energy Environ. Sci.* **2011**, *4*, 3243–3262. [CrossRef]
9. Goriparti, S.; Miele, E.; De Angelis, F.; Di Fabrizio, E.; Zaccaria, R.P.; Capiglia, C. Review on recent progress of nanostructured anode materials for Li-ion batteries. *J. Power Sources* **2014**, *257*, 421–443. [CrossRef]
10. Winter, M.; Brodd, R.J. What are batteries, fuel cells, and supercapacitors? *Chem. Rev.* **2004**, *104*, 4245–4270. [CrossRef]
11. Cheng, F.; Liang, J.; Tao, Z.; Chen, J. Functional materials for rechargeable batteries. *Adv. Mater.* **2011**, *23*, 1695–1715. [CrossRef]
12. Li, H.; Wang, Z.; Chen, L.; Huang, X. Research on advanced materials for Li-ion batteries. *Adv. Mater.* **2009**, *21*, 4593–4607. [CrossRef]
13. Goodenough, J.B.; Kim, Y. Challenges for rechargeable Li batteries. *Chem. Mater.* **2010**, *22*, 587–603. [CrossRef]
14. Tarascon, J.M.; Armand, M. Issues and challenges facing rechargeable lithium batteries. *Nature* **2001**, *414*, 359–367. [CrossRef]
15. Xu, B.; Qian, D.; Wang, Z.; Meng, Y.S. Recent progress in cathode materials research for advanced lithium ion batteries. *Mater. Sci. Eng. R Rep.* **2012**, *73*, 51–65. [CrossRef]
16. Li, J.; Barillas, J.K.; Guenther, C.; Danzer, M.A. A comparative study of state of charge estimation algorithms for LiFePO$_4$ batteries used in electric vehicles. *J. Power Sources* **2013**, *230*, 244–250. [CrossRef]
17. Chacko, S.; Chung, Y.M. Thermal modelling of Li-ion polymer battery for electric vehicle drive cycles. *J. Power Sources* **2012**, *213*, 296–303. [CrossRef]
18. Dunn, J.; Gaines, L.; Kelly, J.; James, C.; Gallagher, K. The significance of Li-ion batteries in electric vehicle life-cycle energy and emissions and recycling's role in its reduction. *Energy Environ. Sci.* **2015**, *8*, 158–168. [CrossRef]
19. Fathabadi, H. Combining a proton exchange membrane fuel cell (PEMFC) stack with a Li-ion battery to supply the power needs of a hybrid electric vehicle. *Renew. Energy* **2019**, *130*, 714–724. [CrossRef]
20. Hannan, M.A.; Hoque, M.M.; Hussain, A.; Yusof, Y.; Ker, P.J. State-of-the-art and energy management system of lithium-ion batteries in electric vehicle applications: Issues and recommendations. *IEEE Access* **2018**, *6*, 19362–19378. [CrossRef]
21. Lin, D.; Liu, Y.; Cui, Y. Reviving the lithium metal anode for high-energy batteries. *Nat. Nanotechnol.* **2017**, *12*, 194–206. [CrossRef]
22. Leisegang, T.; Meutzner, F.; Zschornak, M.; Münchgesang, W.; Schmid, R.; Nestler, T.; Eremin, R.A.; Kabanov, A.A.; Blatov, V.A.; Meyer, D.C. The aluminum-ion battery: A sustainable and seminal concept? *Front. Chem.* **2019**, *7*, 268. [CrossRef] [PubMed]
23. Duehnen, S.; Betz, J.; Kolek, M.; Schmuch, R.; Winter, M.; Placke, T. Toward green battery cells: Perspective on materials and technologies. *Small Methods* **2020**, *4*, 2000039. [CrossRef]
24. Nitta, N.; Yushin, G. High-capacity anode materials for lithium-ion batteries: Choice of elements and structures for active particles. *Part. Part. Syst. Charact.* **2014**, *31*, 317–336. [CrossRef]
25. Obrovac, M.; Christensen, L. Structural changes in silicon anodes during lithium insertion/extraction. *Electrochem. Solid-State Lett.* **2004**, *7*, A93. [CrossRef]
26. Xu, W.; Wang, J.; Ding, F.; Chen, X.; Nasybulin, E.; Zhang, Y.; Zhang, J.G. Lithium metal anodes for rechargeable batteries. *Energy Environ. Sci.* **2014**, *7*, 513–537. [CrossRef]
27. Famprikis, T.; Canepa, P.; Dawson, J.A.; Islam, M.S.; Masquelier, C. Fundamentals of inorganic solid-state electrolytes for batteries. *Nat. Mater.* **2019**, *18*, 1278–1291. [CrossRef]
28. Li, J.; Ma, C.; Chi, M.; Liang, C.; Dudney, N.J. Solid electrolyte: The key for high-voltage lithium batteries. *Adv. Energy Mater.* **2015**, *5*, 1401408. [CrossRef]
29. Sakuda, A.; Kitaura, H.; Hayashi, A.; Tadanaga, K.; Tatsumisago, M. All-solid-state lithium secondary batteries with oxide-coated LiCoO$_2$ electrode and Li$_2$S-P$_2$S$_5$ electrolyte. *J. Power Sources* **2009**, *189*, 527–530. [CrossRef]
30. Sakuda, A.; Hayashi, A.; Tatsumisago, M. Interfacial observation between LiCoO$_2$ electrode and Li$_2$S-P$_2$S$_5$ solid electrolytes of all-solid-state lithium secondary batteries using transmission electron microscopy. *Chem. Mater.* **2010**, *22*, 949–956. [CrossRef]
31. Nagao, M.; Hayashi, A.; Tatsumisago, M.; Kanetsuku, T.; Tsuda, T.; Kuwabata, S. In situ SEM study of a lithium deposition and dissolution mechanism in a bulk-type solid-state cell with a Li$_2$S-P$_2$S$_5$ solid electrolyte. *Phys. Chem. Chem. Phys.* **2013**, *15*, 18600–18606. [CrossRef] [PubMed]
32. Liu, Z.; Fu, W.; Payzant, E.A.; Yu, X.; Wu, Z.; Dudney, N.J.; Kiggans, J.; Hong, K.; Rondinone, A.J.; Liang, C. Anomalous high ionic conductivity of nanoporous $\beta$-Li$_3$PS$_4$. *J. Am. Chem. Soc.* **2013**, *135*, 975–978. [CrossRef] [PubMed]
33. Lepley, N.; Holzwarth, N. Modeling interfaces between solids: Application to Li battery materials. *Phys. Rev. B* **2015**, *92*, 214201. [CrossRef]

34. Wenzel, S.; Weber, D.A.; Leichtweiss, T.; Busche, M.R.; Sann, J.; Janek, J. Interphase formation and degradation of charge transfer kinetics between a lithium metal anode and highly crystalline $Li_7P_3S_{11}$ solid electrolyte. *Solid State Ionics* **2016**, *286*, 24–33. [CrossRef]

35. Rangasamy, E.; Liu, Z.; Gobet, M.; Pilar, K.; Sahu, G.; Zhou, W.; Wu, H.; Greenbaum, S.; Liang, C. An iodide-based $Li_7P_2S_8I$ superionic conductor. *J. Am. Chem. Soc.* **2015**, *137*, 1384–1387. [CrossRef] [PubMed]

36. Wenzel, S.; Sedlmaier, S.J.; Dietrich, C.; Zeier, W.G.; Janek, J. Interfacial reactivity and interphase growth of argyrodite solid electrolytes at lithium metal electrodes. *Solid State Ionics* **2018**, *318*, 102–112. [CrossRef]

37. Mayo, M.; Griffith, K.J.; Pickard, C.J.; Morris, A.J. Ab initio study of phosphorus anodes for lithium-and sodium-ion batteries. *Chem. Mater.* **2016**, *28*, 2011–2021. [CrossRef]

38. Li, L.; Yu, Y.; Ye, G.J.; Ge, Q.; Ou, X.; Wu, H.; Feng, D.; Chen, X.H.; Zhang, Y. Black phosphorus field-effect transistors. *Nat. Nanotechnol.* **2014**, *9*, 372–377. [CrossRef]

39. Kulish, V.V.; Malyi, O.I.; Persson, C.; Wu, P. Phosphorene as an anode material for Na-ion batteries: A first-principles study. *Phys. Chem. Chem. Phys.* **2015**, *17*, 13921–13928. [CrossRef]

40. Zhao, S.; Kang, W.; Xue, J. The potential application of phosphorene as an anode material in Li-ion batteries. *J. Mater. Chem. A* **2014**, *2*, 19046–19052. [CrossRef]

41. Sun, J.; Lee, H.W.; Pasta, M.; Yuan, H.; Zheng, G.; Sun, Y.; Li, Y.; Cui, Y. A phosphorene–graphene hybrid material as a high-capacity anode for sodium-ion batteries. *Nat. Nanotechnol.* **2015**, *10*, 980–985. [CrossRef]

42. Fu, Y.; Wei, Q.; Zhang, G.; Sun, S. Advanced phosphorus-based materials for lithium/sodium-ion batteries: Recent developments and future perspectives. *Adv. Energy Mater.* **2018**, *8*, 1703058. [CrossRef]

43. Amine, R.; Daali, A.; Zhou, X.; Liu, X.; Liu, Y.; Ren, Y.; Zhang, X.; Zhu, L.; Al-Hallaj, S.; Chen, Z.; et al. A practical phosphorus-based anode material for high-energy lithium-ion batteries. *Nano Energy* **2020**, *74*, 104849. [CrossRef]

44. Fang, K.; Liu, D.; Xiang, X.; Zhu, X.; Tang, H.; Qu, D.; Xie, Z.; Li, J.; Qu, D. Air-stable red phosphorus anode for potassium/sodium-ion batteries enabled through dual-protection design. *Nano Energy* **2020**, *69*, 104451. [CrossRef]

45. Feng, W.; Wang, H.; Jiang, Y.; Zhang, H.; Luo, W.; Chen, W.; Shen, C.; Wang, C.; Wu, J.; Mai, L. A Strain-Relaxation Red Phosphorus Freestanding Anode for Non-Aqueous Potassium Ion Batteries. *Adv. Energy Mater.* **2022**, *12*, 2103343. [CrossRef]

46. Kresse, G.; Furthmüller, J. Efficient iterative schemes for ab initio total-energy calculations using a plane-wave basis set. *Phys. Rev. B* **1996**, *54*, 11169. [CrossRef]

47. Kresse, G.; Furthmüller, J. Efficiency of ab-initio total energy calculations for metals and semiconductors using a plane-wave basis set. *Comput. Mater. Sci.* **1996**, *6*, 15–50. [CrossRef]

48. Blöchl, P.E. Projector augmented-wave method. *Phys. Rev. B* **1994**, *50*, 17953. [CrossRef] [PubMed]

49. Kresse, G.; Joubert, D. From ultrasoft pseudopotentials to the projector augmented-wave method. *Phys. Rev. B* **1999**, *59*, 1758. [CrossRef]

50. Perdew, J.P.; Burke, K.; Ernzerhof, M. Generalized gradient approximation made simple. *Phys. Rev. Lett.* **1996**, *77*, 3865. [CrossRef]

51. Parlinski, K.; Li, Z.Q.; Kawazoe, Y. First-Principles Determination of the Soft Mode in Cubic $ZrO_2$. *Phys. Rev. Lett.* **1997**, *78*, 4063–4066. [CrossRef]

52. Togo, A.; Tanaka, I. First principles phonon calculations in materials science. *Scr. Mater.* **2015**, *108*, 1–5. j.scriptamat.2015.07.021. [CrossRef]

53. Kresse, G.; Hafner, J. Ab initio molecular dynamics for liquid metals. *Phys. Rev. B* **1993**, *47*, 558. [CrossRef]

54. Evans, D.J. Computer "experiment" for nonlinear thermodynamics of Couette flow. *J. Chem. Phys.* **1983**, *78*, 3297–3302. [CrossRef]

55. Hoover, W.G.; Ladd, A.J.; Moran, B. High-strain-rate plastic flow studied via nonequilibrium molecular dynamics. *Phys. Rev. Lett.* **1982**, *48*, 1818. [CrossRef]

56. Shapeev, A.V. Moment tensor potentials: A class of systematically improvable interatomic potentials. *Multiscale Model. Simul.* **2016**, *14*, 1153–1173. [CrossRef]

57. Zuo, Y.; Chen, C.; Li, X.; Deng, Z.; Chen, Y.; Behler, J.; Csányi, G.; Shapeev, A.V.; Thompson, A.P.; Wood, M.A.; et al. Performance and cost assessment of machine learning interatomic potentials. *J. Phys. Chem. A* **2020**, *124*, 731–745. [CrossRef] [PubMed]

58. Podryabinkin, E.V.; Tikhonov, E.V.; Shapeev, A.V.; Oganov, A.R. Accelerating crystal structure prediction by machine-learning interatomic potentials with active learning. *Phys. Rev. B* **2019**, *99*, 064114. [CrossRef]

59. Körmann, F.; Kostiuchenko, T.; Shapeev, A.; Neugebauer, J. B2 ordering in body-centered-cubic AlNbTiV refractory high-entropy alloys. *Phys. Rev. Mater.* **2021**, *5*, 053803. [CrossRef]

60. Shapeev, A.V.; Podryabinkin, E.V.; Gubaev, K.; Tasnádi, F.; Abrikosov, I.A. Elinvar effect in $\beta$-Ti simulated by on-the-fly trained moment tensor potential. *New J. Phys.* **2020**, *22*, 113005. [CrossRef]

61. Novoselov, I.; Yanilkin, A.; Shapeev, A.; Podryabinkin, E. Moment tensor potentials as a promising tool to study diffusion processes. *Comput. Mater. Sci.* **2019**, *164*, 46–56. [CrossRef]

62. Novikov, I.S.; Suleimanov, Y.V.; Shapeev, A.V. Automated calculation of thermal rate coefficients using ring polymer molecular dynamics and machine-learning interatomic potentials with active learning. *Phys. Chem. Chem. Phys.* **2018**, *20*, 29503–29512. [CrossRef]

63. Rosenbrock, C.W.; Gubaev, K.; Shapeev, A.V.; Pártay, L.B.; Bernstein, N.; Csányi, G.; Hart, G.L. Machine-learned interatomic potentials for alloys and alloy phase diagrams. *NPJ Comput. Mater.* **2021**, *7*, 24. [CrossRef]

64. Novikov, I.S.; Gubaev, K.; Podryabinkin, E.V.; Shapeev, A.V. The MLIP package: Moment tensor potentials with MPI and active learning. *Mach. Learn. Sci. Technol.* **2020**, *2*, 025002. [CrossRef]

65. Podryabinkin, E.V.; Shapeev, A.V. Active learning of linearly parametrized interatomic potentials. *Comput. Mater. Sci.* **2017**, *140*, 171–180. [CrossRef]

66. Plimpton, S. Fast parallel algorithms for short-range molecular dynamics. *J. Comput. Phys.* **1995**, *117*, 1–19. [CrossRef]

67. Thompson, A.P.; Aktulga, H.M.; Berger, R.; Bolintineanu, D.S.; Brown, W.M.; Crozier, P.S.; in't Veld, P.J.; Kohlmeyer, A.; Moore, S.G.; Nguyen, T.D.; et al. LAMMPS—A flexible simulation tool for particle-based materials modeling at the atomic, meso, and continuum scales. *Comput. Phys. Commun.* **2022**, *271*, 108171. [CrossRef]

68. Hoover, W.G. Constant-pressure equations of motion. *Phys. Rev. A* **1986**, *34*, 2499. [CrossRef] [PubMed]

69. Evans, D.J.; Holian, B.L. The nose–hoover thermostat. *J. Chem. Phys.* **1985**, *83*, 4069–4074. [CrossRef]

70. Saal, J.E.; Kirklin, S.; Aykol, M.; Meredig, B.; Wolverton, C. Materials design and discovery with high-throughput density functional theory: The open quantum materials database (OQMD). *Jom* **2013**, *65*, 1501–1509. [CrossRef]

71. Kirklin, S.; Saal, J.E.; Meredig, B.; Thompson, A.; Doak, J.W.; Aykol, M.; Rühl, S.; Wolverton, C. The Open Quantum Materials Database (OQMD): Assessing the accuracy of DFT formation energies. *NPJ Comput. Mater.* **2015**, *1*, 15010. [CrossRef]

72. Jain, A.; Ong, S.P.; Hautier, G.; Chen, W.; Richards, W.D.; Dacek, S.; Cholia, S.; Gunter, D.; Skinner, D.; Ceder, G.; et al. Commentary: The Materials Project: A materials genome approach to accelerating materials innovation. *APL Mater.* **2013**, *1*, 011002. [CrossRef]

73. Sen, R.; Johari, P. Comment on "Structure Prediction of Li-Sn and Li-Sb Intermetallics for Lithium-Ion Batteries Anodes". *arXiv* **2018**, arXiv:1807.10540.

74. Mayo, M.; Morris, A.J. Structure prediction of Li–Sn and Li–Sb intermetallics for lithium-ion batteries anodes. *Chem. Mater.* **2017**, *29*, 5787–5795. [CrossRef]

75. Fei, G.; Duan, S.; Zhang, M.; Ren, Z.; Cui, Y.; Chen, X.; Liu, Y.; Yi, W.; Liu, X. Predicted stable $Li_5P_2$ and $Li_4P$ at ambient pressure: Novel high-performance anodes for lithium-ion batteries. *Phys. Chem. Chem. Phys.* **2020**, *22*, 19172–19177. [CrossRef] [PubMed]

76. Oganov, A. R.; Glass, C. W. Crystal structure prediction using ab initio evolutionary techniques: Principles and applications. *He J. Chem. Phys.* **2006**, *124*, 244704. [CrossRef] [PubMed]

77. Oganov, A. R.; Lyakhov, A. O.; Valle, M. How Evolutionary Crystal Structure Prediction Works and Why. *Acc. Chem. Res.* **2011**, *44*, 227–237. [CrossRef] [PubMed]

78. Lyakhov, A. O.; Oganov, A. R.; Stokes, H. T.; Zhu, Q. New developments in evolutionary structure prediction algorithm USPEX. *Comput. Phys. Commun.* **2013**, *4*, 1172–1182. [CrossRef]

79. Dong, Y.; DiSalvo, F.J. Reinvestigation of trilithium phosphide, $Li_3P$. *Acta Crystallogr. Sect. E Struct. Rep. Online* **2007**, *63*, i97–i98. [CrossRef]

80. Hönle, W.; von Schnering, H.G. Chemistry and Structural Chemistry of Phosphides and Polyphosphides 23* Zur Struktur von LiP und KSb. *Z. Krist. Cryst. Mater.* **1981**, *155*, 307–314. [CrossRef]

81. Manriquez, V.; Hönle, W.; von Schnering, H.G. Zur Chemie und Strukturchemie von Phosphiden und Polyphosphiden. 42. Trilithiumheptaphosphid $Li_3P_7$: Darstellung, Struktur und Eigenschaften. *Z. Anorg. Allg. Chem.* **1986**, *539*, 95–109. [CrossRef]

82. Wichelhaus, W. Die Lithiumphosphide $LiP_5$ und $LiP_7$. *Naturwissenschaften* **1972**, *59*, 78–79.

83. Ozisik, H.; Colakoglu, K.; Deligoz, E.; Ozisik, H. First principles study on the structural, electronic, and elastic properties of Na–As systems. *Solid State Commun.* **2011**, *151*, 1349–1354. [CrossRef]

84. Wegner, F.; Kamm, F.; Pielnhofer, F.; Pfitzner, A. $Li_3As$ and $Li_3P$ revisited: DFT modelling on phase stability and ion conductivity. *Z. Anorg. Allg. Chem.* **2022**, *648*, e202100358.

85. Nazri, G. Preparation, structure and ionic conductivity of lithium phosphide. *Solid State Ionics* **1989**, *34*, 97–102. [CrossRef]